

Quantum Simulation of Operator Spreading in the Chaotic Ising Model

Michael R. Geller,^{1,*} Andrew Arrasmith,² Zoë Holmes,³ Bin Yan,^{4,2} Patrick J. Coles,² and Andrew Sornborger^{3,†}

¹*Center for Simulational Physics, University of Georgia, Athens, Georgia 30602, USA*

²*Theoretical Division, Los Alamos National Laboratory, Los Alamos, NM, USA.*

³*Information Sciences, Los Alamos National Laboratory, Los Alamos, NM, USA.*

⁴*Center for Nonlinear Studies, Los Alamos National Laboratory, Los Alamos, NM, USA.*

(Dated: July 8, 2021)

There is great interest in using near-term quantum computers to simulate and study foundational problems in quantum mechanics and quantum information science, such as the scrambling measured by an out-of-time-ordered correlator (OTOC). Here we use an IBM Q processor, quantum error mitigation, and *weaved* Trotter simulation to study high-resolution operator spreading in a 4-spin Ising model as a function of space, time, and integrability. Reaching 4 spins while retaining high circuit fidelity is made possible by the use of a physically motivated fixed-node variant of the OTOC, allowing scrambling to be estimated without overhead. We find clear signatures of ballistic operator spreading in a chaotic regime, as well as operator localization in an integrable regime. The techniques developed and demonstrated here open up the possibility of using cloud-based quantum computers to study and visualize scrambling phenomena, as well as quantum information dynamics more generally.

A key concept in modern quantum physics is the non-commutativity of operators corresponding to physically separated local observables W and V caused by scrambling. Scrambling is a spreading of quantum information over many degrees of freedom, generated by chaotic unitary evolution [1]. The resulting growth of an operator $W(t) = e^{iHt}W e^{-iHt}$ in time can be diagnosed by the nonvanishing of the “commutator” [2–9]

$$\begin{aligned} \text{tr}[\rho|[W(t), V(0)]|^2] &= \text{tr}[\rho W(t)V(0)V(0)W(t)] \\ &+ \text{tr}[\rho V(0)W(t)W(t)V(0)] - 2\text{Re } F(t) \end{aligned} \quad (1)$$

in some state ρ (often a thermal state). Here

$$F(t) = \text{tr}[\rho W(t)V(0)W(t)V(0)] \quad (2)$$

is the out-of-time-ordered correlator (OTOC). The theoretical study of scrambling and OTOCs has enhanced our understanding of entanglement in condensed matter, quantum field theory, and quantum gravity [10–28].

Fast scrambling appears in a variety of systems, including black holes [2–5] and strange metals [6, 7], while slow scrambling indicates a breakdown of ergodicity and thermalization [8, 9]. However, the dynamics of information away from these two extremes, such as operator spreading in ordinary quantum matter, is less well understood [24, 25]. Open problems also include predicting the scrambling generated by a given model Hamiltonian (without simulating it) [25], the nature of scrambling in models without particle-like classical limits [24–27], and determining when a fast scrambler has a dual description as a black hole [1]. Additional questions that can be addressed with the techniques developed here include the dependence of scrambling on ρ , the dependence on W and V , and the difference between thermal scrambling in

gapped and gapless phases, such as integer versus half-integer-spin 1d antiferromagnets (with or without the Haldane gap [29]).

Direct experimental measurement of (1) is challenging because it requires reversing the direction of time (changing the sign of the Hamiltonian) during the experiment. But it can be simulated on a classical or quantum computer. While classical simulation is limited to small or weakly correlated models, fault-tolerant quantum computers promise to make large-scale scrambling simulations practical. This should provide a valuable tool for quantum information science by complimenting the study of solvable models [2–9]. However, near-term quantum simulations are restricted to a small number of qubits and short circuits. Online users may also face additional restrictions that limit the number of distinct quantum circuits that can be measured, and thus the overall complexity of an experiment and the resulting data quality.

The quantum simulation of scrambling with near-term processors is especially challenging because, at each time t , four Hamiltonian simulations of length t are implemented to calculate F , two each moving forward and backward in time. In addition, F is complex so it has to be measured interferometrically [30–32], requiring extra qubits and gates, or via weak measurement [33], which is not widely available. It is also possible to measure scrambling via correlations between randomized measurements [18]. But achieving an accurate simulation over long times with high time resolution is difficult with standard Trotter simulation [34–45]. We introduce techniques to address these limitations and help enable the study and visualization of quantum information dynamics with cloud-based quantum computers.

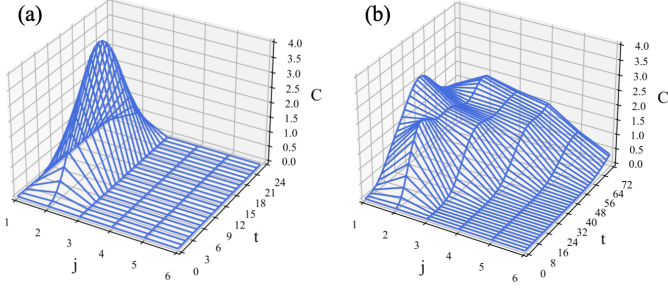


FIG. 1. Commutator $C_{1j}(t)$ versus qubit position j and time t . (a) Integrable regime, where no spreading occurs. The OTOC is calculated at times $t \in \{0, \tau, 2\tau, \dots, 24\tau\}$, with resolution $\tau = 0.06$, and time is plotted in units of τ . (b) Chaotic regime, calculated with $\tau = 0.03$, showing ballistic operator spreading. Parameters for both regimes are given in Table I.

The first quantum simulations of an OTOC were made by Li *et al.* [46] on a nuclear magnetic resonance simulator and by Gärttner *et al.* [47] on a long-range Ising spin simulator. Since then, the experimental study of scrambling has made impressive progress [48–58], including recent striking demonstrations of teleportation-based OTOC measurement [50, 51], which distinguishes OTOC decay due to unitary scrambling from decoherence, and Google’s measurement of OTOC fluctuations on random circuits containing up to 53 qubits [54], which distinguishes operator entanglement from spreading. Google also measured operator spreading in a 2d array of qubits [54].

In this work we use quantum simulation techniques to study spreading of the Pauli operator $X(t) = e^{iHt} X e^{-iHt}$ in the Ising chain

$$H = H^0 + B_x \sum_{i=1}^n X_i, \quad (3)$$

$$H^0 = J \sum_{i=1}^{n-1} Z_i Z_{i+1} + B_z \sum_{i=1}^n Z_i, \quad (4)$$

with n spins. The model is separated into a classical Ising chain H^0 plus a noncommuting transverse field. The model (3) permits efficient Hamiltonian simulation via Trotterization. H^0 is also exactly solvable, a property used below. We measure and plot the commutator

$$C_{ij}(t) = \text{tr}(\rho [X_i(t), X_j(0)]^2) = 2 - 2 \text{Re } F_{ij}(t), \quad (5)$$

in the state $\rho = |0000\rangle\langle 0000|$, with $X(t)$ initially localized at $i=1$. In particular, we study C_{1j} as a function of qubit position $j \in \{1, 2, \dots, N\}$ and time t . The quantum simulations are implemented on the IBM Q processor ibmq_sydney using qubits $\{Q_1, Q_2, Q_3, Q_5\}$ [59]. The measured OTOC is

$$F_{1j}(t) = \langle 0000 | U^\dagger X_1 U X_j U^\dagger X_1 U X_j | 0000 \rangle, \quad (6)$$

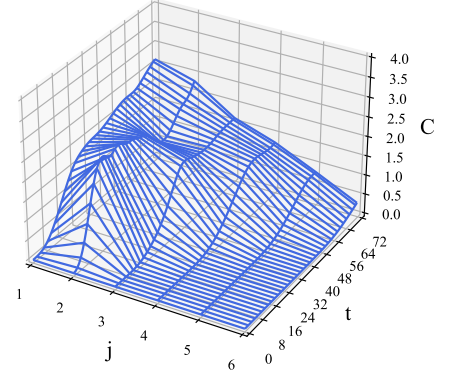


FIG. 2. Chaotic $C_{1j}(t)$ commutator of Fig. 1b recalculated with the fixed-node OTOC.

where U is a 4-qubit circuit simulating e^{-iHt} . The commutator (5) was chosen because it exhibits a particularly smooth, easily visualized dynamics, using an easy-to-prepare state. Operator spreading diagnosed by alternative commutators are compared in [59].

In the experiments we always use one of the two parameter sets given in Table I, both of which simulate ferromagnetic spin chains. One set corresponds to an integrable regime of the dynamics; the other generates quantum chaos, which causes unitary OTOC decay. The models are chosen to display smooth charge spreading dynamics on the timescales of interest. The measurements in the integrable regime are relevant for recent theoretical work investigating the role of integrability on scrambling [24, 26], as well as serving as a scrambling-free experimental control. The commutator (5) is a real number $0 \leq C_{1j}(t) \leq 4$, and can be represented by a surface in spacetime $j \times t$. Figure 1 shows two such surfaces, obtained by classical simulation, for $n = 6$. These simulations assume perfect Hamiltonian simulation $U = e^{-iHt}$ with no Trotter error. Operator localization in Fig. 1a and spreading in Fig. 1b are evident. These high-resolution simulations allow one to investigate operator spreading dynamics in great detail.

TABLE I. Ising model parameters.

	J	B_x	B_z
Integrable regime	-1	0	1
Chaotic regime	-1	0.7	1.5

Fixed-node OTOC. A standard approach to measuring an OTOC on n qubits is to add a qubit that can control the W and V gates [30, 31]. Here we introduce an alternative approach, which is approximate but allows one to reach larger problem sizes. Writing the OTOC

in polar form as $F_{ij} = e^{i \arg F_{ij}} |F_{ij}|$, we note that the phase becomes irrelevant in the scrambling regime, because $|F_{ij}| \approx 0$ there. $|F_{ij}|$ can be measured directly with no qubit overhead [30], at least on simple states. Therefore we introduce an approximation for $\arg F_{ij}$ that is exact in the integrable regime, namely $\arg F_{ij}^0$, where F_{ij}^0 is the OTOC calculated with the classical Hamiltonian H^0 . For the Ising model (3),

$$F_{1j}^0(t) = \begin{cases} e^{4i(J+B_z)t} & \text{if } j = 1, \\ e^{4iJt} & \text{if } j = 2, \\ 1 & \text{if } j > 2. \end{cases} \quad (7)$$

This results in a *fixed-node* variant of the OTOC,

$$F_{ij} = e^{i \arg F_{ij}^0} |F_{ij}|. \quad (8)$$

One can think of the fixed-node OTOC as an approximation to (2), or as an independent quantity that also diagnoses scrambling.

Using the fixed-node OTOC, the commutator takes the form

$$C_{ij} = 2 - 2|F_{ij}| \cos(\arg F_{ij}^0). \quad (9)$$

The chaotic surface of Fig. 1b, recalculated with the fixed-node OTOC, is shown in Fig. 2.

By construction, the fixed-node OTOC is close to the exact OTOC in the late time regime, where $F_{ij} \approx 0$ ($C_{ij} \approx 2$). However, it also satisfies an important *causality* constraint that extends its accuracy to the regime of $F_{ij} \approx 1$ ($C_{ij} \approx 0$) as well, namely, the early scrambling regime. Causality requires that the exact OTOC satisfies $F_{ij} = 1$ outside the *lightcone*, i.e. when $|\mathbf{r}_i - \mathbf{r}_j| > vt$, with $\mathbf{r}_{i,j}$ the local operator positions and v the butterfly velocity. Therefore $\arg(F_{ij}) = 0$ there. Because F_{ij}^0 also satisfies this constraint, C_{ij} computed from the fixed-node OTOC is also accurate outside the lightcone, as is evident in Fig. 2. Thus, while there are small differences in the peak structure in $C_{1j}(t)$, mainly at $j = 1$, the overall spreading dynamics is accurately captured. The fixed-node commutator in the integrable regime is identical to the surface of Fig. 1a.

Trotter weave. To measure $C_{ij}(t)$ with the high time resolution used in Fig. 1, one might construct a Trotter approximation $U(\tau) \approx e^{-iH\tau}$ for evolution by a short time τ . Then, to simulate later times $t = \ell\tau$, the operator $U(\tau)$ is applied ℓ times:

$$e^{-iH\ell\tau} \approx U(\tau)^\ell. \quad (10)$$

The value of τ determines the time resolution. However, the circuit depth resulting from this standard Trotterization, based on the repeated application of a single step $U(\tau)$, is t/τ . Thus, the performance of (10) quickly degrades with t due to gate errors and decoherence, limiting the simulation to short times. We address this by an extension of Trotter simulation based on a collection of elementary evolution operators.

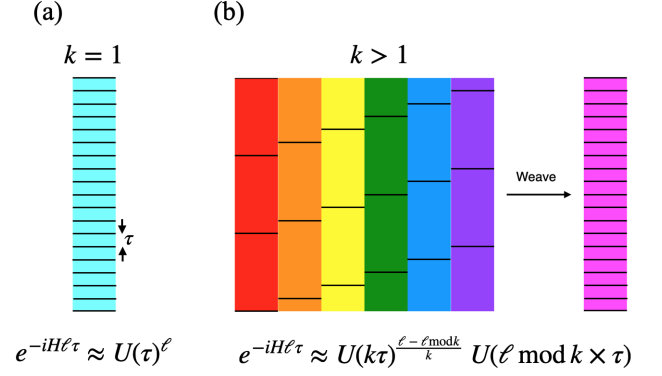


FIG. 3. (Color online) Weaved time evolution. (a) Standard Trotter method, where a step $U(\tau)$ is repeatedly applied. (b) Weaving implements a fine-grained time evolution, with time resolution τ , without incurring the gate errors of (a). Here the red column represents the sequence $U(k\tau) \cdots U(k\tau)$, orange represents $U(k\tau) \cdots U(k\tau)U(\tau)$, yellow represents $U(k\tau) \cdots U(k\tau)U(2\tau)$ and purple represents $U(k\tau) \cdots U(k\tau)U((k-1)\tau)$.

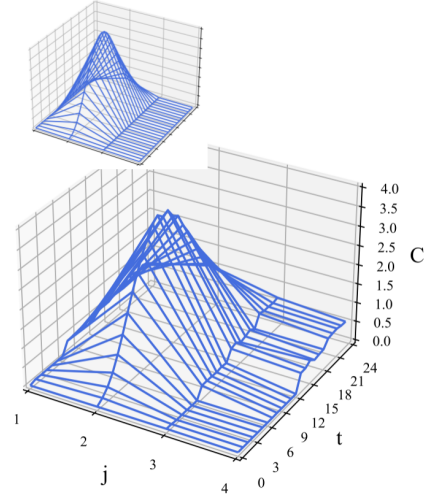


FIG. 4. (Color online) Measured operator spreading surface in the integral regime, using the fixed-node OTOC. The main figure uses a 6-weave with $\tau = 0.06$, and includes both CNOT and measurement error mitigation. C_{1j} is defined in (5), with $j \in \{1, 2, 3, 4\}$ the coordinate of the probe qubit. The OTOC is measured at times $t \in \{0, \tau, 2\tau, 3\tau, \dots, 24\tau\}$, and time is plotted in units of τ . The inset shows the classically computed noise-free surface.

A *k-weave* is a set of k unitaries

$$\left\{ U(\tau), U(2\tau), \dots, U(k\tau) \right\}, \quad (11)$$

where τ is a fixed short evolution time and each $U(dt)$ is a Trotterized evolution operator, propagating a state for a short time dt . The integer $k \in \{1, 2, 3, \dots\}$ is called the weave modulus. The unitaries in (11) have different roles: $U(k\tau)$ is the *cell* operator and the remaining

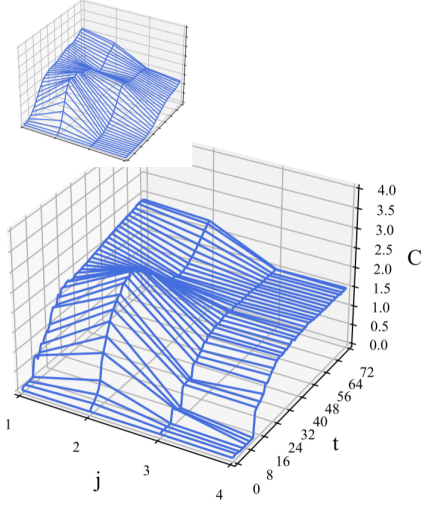


FIG. 5. (Color online) Operator spreading in the chaotic regime using the fixed-node OTOC. We use a 6-weave with $\tau = 0.03$, and also include error mitigation. The OTOC is measured at times $t \in \{0, \tau, 2\tau, \dots, 72\tau\}$. The inset shows the noise-free surface.

$k - 1$ unitaries are called *shift* operators. Repeated applications of the cell propagates a state from $t = 0$ to a time $t = (\ell - \ell \bmod k) \times \tau$, but with coarse time resolution $k\tau$. The coarse evolution is then followed (or preceded) by a single shift operator propagating for a short interval with fine-grained time precision τ . Instead of (10), weaving implements a time evolution according to

$$e^{-iH\ell\tau} \approx U(k\tau)^{\frac{\ell - \ell \bmod k}{k}} U(\ell \bmod k \times \tau), \quad (12)$$

where the cell operator is applied $(\ell - \ell \bmod k)/k$ times after a single shift operator. This is illustrated in Fig. 3. When $\ell \gg k$, this leads to a k -fold reduction in circuit depth, and to higher circuit fidelity, at the expense of increased of Trotter error. Weaving can be applied to Hamiltonian simulation techniques beyond Trotterization as well.

For our first set of measurements we use the weave operators $\{U(\ell\tau)\}_{\ell=1}^k$, where

$$U(\ell\tau) = \prod_{i=1}^n R_x(B_x \ell\tau)_i \times \prod_{i=1}^{n-1} R_{zz}(2J\ell\tau)_{i,i+1} \times \prod_{i=1}^n P_z(2B_z \ell\tau)_i \times \prod_{i=1}^n R_x(B_x \ell\tau)_i, \quad (13)$$

resulting from a Trotterization of the model (3). Here $R_x(\theta)_i = e^{-i\theta X_i/2}$ is a rotation on qubit i ,

$$R_{zz}(\theta)_{ij} = e^{-i\frac{\theta}{2} Z_i \otimes Z_j} = \text{CNOT}_{ij} P_z(\theta)_i \text{CNOT}_{ij} \quad (14)$$

is a ZZ rotation, $P_z(\varphi) = \text{diag}(1, e^{i\varphi})$ is a phase gate, and CNOT_{ij} is an X on qubit j controlled by i . For general angles θ , $R_{zz}(\theta)_{ij}$ requires two CNOTs per graph edge,

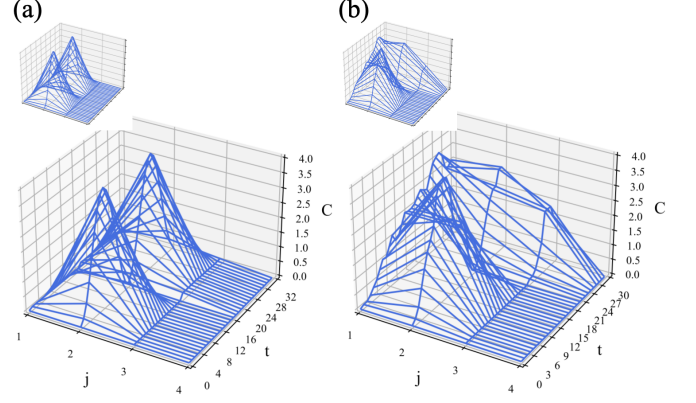


FIG. 6. (Color online) Measured operator spreading surfaces using the fixed-node OTOC and magic cell operator. (a) 16-weave in the integrable regime with $\tau = 0.098$ and up to 32 steps. (b) 20-weave in the chaotic regime with $\tau = 0.079$ and up to 30 steps. Insets show the noise-free surfaces.

or $2(n - 1)$ CNOTs per Trotter step on a chain of length n . The quantum simulation results reported here use (up to) two weave operators per Hamiltonian simulation, requiring $4(n - 1)$ CNOTs per evolution. This leads to a total of $16(n - 1)$ CNOTs per OTOC simulation (48 CNOTs for $n = 4$).

Results. All of the quantum simulation results in this study were obtained with the IBM Q processor *ibmq-sydney* on the 4-qubit chain $\{Q_1, Q_2, Q_3, Q_5\}$ [59]. Quantum simulations using Trotter weave modulus $k = 6$ are shown in Figs. 4 and 5. Figure 4 shows the measured spreading surface $C_{1j}(t)$ in an integral regime of the spin chain. Figure 5 is the same, but calculated in a chaotic regime of the model. The parameter values used are shown in Table I. The data in both regimes are corrected for measurement errors using transition matrix error mitigation [60–64], and for incoherent CNOT errors using zero-noise extrapolation [65, 66]. The raw data from this study is provided in [59].

The values of τ (time resolution) and k (weave modulus) are chosen to balance gate errors and Trotter errors over the relevant time scales of the simulation. In particular, τ has to be small enough to resolve the oscillations in the peaks of the spreading surfaces (see Figs. 1 and 2). However, τ also has to be large enough to enable simulations that probe the long-time spreading dynamics. A large value of k is desirable because it enables longer simulations, as fewer applications of the cell circuit are required. But a large value of k also leads to larger Trotter errors in the weave operators.

Magic cell. In many weaving applications, the largest Trotter error will come from the cell $U(k\tau)$, because its evolution time $k\tau$ is largest. However, some simulations admit simplified Trotter steps $U(dt)$ for certain “magic” values of dt . In the Ising chain, for example, this occurs

when $2Jdt = \pm\frac{\pi}{2}$, because for these angles we can use the decomposition

$$R_{zz}(\frac{\pi}{2})_{ij} = e^{-i\frac{\pi}{4}Z_i \otimes Z_j} = e^{-i\frac{\pi}{4}} S_i S_j CZ_{ij}, \quad (15)$$

or its Hermitian conjugate, instead of (14). Here $S = \text{diag}(1, e^{i\frac{\pi}{2}})$ and CZ is a controlled-Z gate that can be implemented using a single CNOT and two Hadamard gates. This leads to a two-fold reduction in the number of CNOTs required. We demonstrate this variation, where the weave is built around a *magic* cell operator with evolution time $dt_{\text{magic}} = k\tau = \pi/4|J|$. Because dt_{magic} is now fixed to a special value, the use of a magic cell imposes a constraint $dt_{\text{magic}} = k\tau$ on k and τ ; they are no longer independent. Operator spreading measurements using a 16-weave with magic cell in the integrable regime, and a 20-weave with magic cell in the chaotic regime, are shown in Fig. 6. The parameter values used are shown in Table I. The data in both regimes are error mitigated. The benefits of using a magic cell here are modest, because we only apply it once. However, the use of a magic cell has the potential to significantly extend the range of Trotterized quantum simulation as gate errors improve and larger circuits become possible.

Conclusions. Recent experiments have established that scrambling can be simulated with current gate-based quantum computers [50–58], making it possible to investigate interesting unsolved problems at the intersection of quantum information and physics. In this work we introduce and demonstrate techniques to enable high-resolution operator spreading measurements with cloud-based quantum computers. Trotter weaving provides the high time resolution, and the fixed-node OTOC enables larger problem sizes. Both approaches are practical for online users and have applications elsewhere in quantum information science. We observe clear signatures of operator spreading in a chaotic regime of a 4-qubit Ising model, as well as operator localization in an integrable regime. These techniques help make it possible to study information dynamics in strongly correlated and highly entangled quantum systems.

Acknowledgments. We thank Andreas Albrecht for useful discussions. PJC and AS acknowledge initial support and MRG acknowledges support from LANL’s Laboratory Directed Research and Development (LDRD) program under project number 20190065DR. AA and ZH acknowledge, and PJC and AS acknowledge (subsequent to the above acknowledged funding) that this work was supported by the U.S. Department of Energy, Office of Science, Office of High Energy Physics QuantISED program under Contract No. KA2401032. ZH acknowledges support from the LANL LDRD-funded Mark Kac Postdoctoral Fellowship. BY acknowledges support of the U.S. Department of Energy, Office of Science, Basic Energy Sciences, Materials Sciences and Engineering Division, Condensed Matter Theory Program, and partial support from the Center for Nonlinear Studies.

Supplementary Information for “Quantum Simulation of Operator Spreading in the Chaotic Ising Model”

This document provides additional details about the experimental results. Section 1 describes the online superconducting qubits used, and gives calibration results (gate errors, coherence times, and single-qubit measurement errors) provided by the backend. Section 2 presents raw data. In Sec. 3 we discuss the error mitigation techniques used and their effect on the data. In Sec. 4 we calculate the OTOC for the classical Ising model H^0 . Alternative OTOCs are discussed in Sec. 5.

1. QUBITS

In this section we discuss the online superconducting qubits used in this work. Data was taken on the IBM Q processor `ibmq_sydney` using the BQP software package developed by the authors. We measure the OTOC on qubits $\{Q_1, Q_2, Q_3, Q_5\}$ shown in Fig. S1. Calibration data supplied by the backend is summarized in Table I. Here $T_{1,2}$ are the standard Markovian decoherence times, and

$$\epsilon = \frac{T(0|1) + T(1|0)}{2} \quad (\text{S1})$$

is the single-qubit state-preparation and measurement (SPAM) error, averaged over initial classical states. $T(0|1)$ is the probability of measuring a $|0\rangle$ state after preparing $|1\rangle$; $T(1|0)$ is the reverse. The U_2 error column gives the single-qubit gate error measured by randomized benchmarking. The reported CNOT errors are also measured by randomized benchmarking.

TABLE I. Calibration data provided by IBM Q for the `ibmq_sydney` chip during the period of data acquisition.

Qubit	T_1 (μs)	T_2 (μs)	SPAM error ϵ	U_2 error
Q_1	99.7	37.3	0.043	2.83e-4
Q_2	107.9	65.5	0.015	1.80e-4
Q_3	78.7	51.7	0.017	3.15e-4
Q_5	147.4	61.1	0.017	1.64e-4
CNOT gates			CNOT error	
CNOT _{1,2}		CNOT _{2,1}	7.67e-3	
CNOT _{2,3}		CNOT _{3,2}	7.00e-3	
CNOT _{3,5}		CNOT _{5,3}	7.68e-3	

2. RAW OPERATOR SPREADING DATA

The raw operator spreading surfaces are shown in Figs. S2 and S3. The differences between the raw and error-mitigated data are shown in Sec. 3.

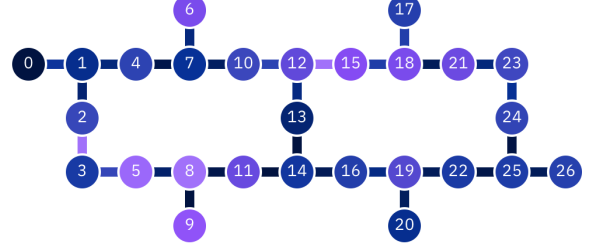


FIG. S1. Layout of IBM Q device `ibmq_sydney`. In this work we use qubits Q_1 , Q_2 , Q_3 and Q_5 .

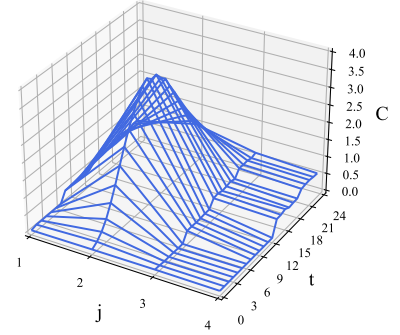


FIG. S2. Raw spreading data in the integral regime, with the same settings as in Fig. 4.

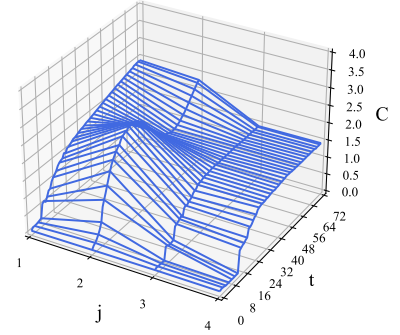


FIG. S3. Raw spreading data in the chaotic regime, with the same settings as in Fig. 5.

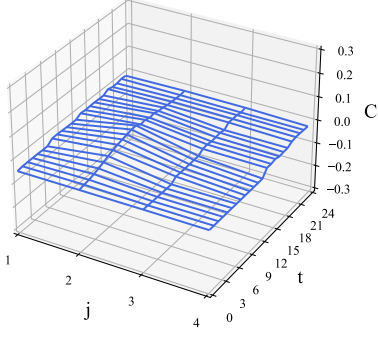


FIG. S4. Difference $C_{\text{TMEM}} - C_{\text{raw}}$ between measurement-corrected and raw surfaces in the integrable regime.

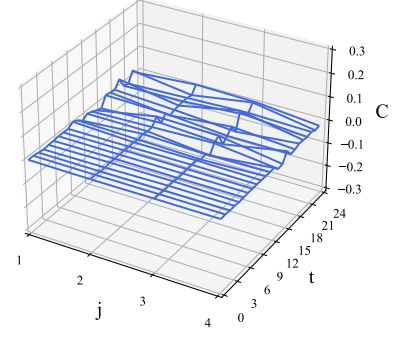


FIG. S6. Difference $C_{\text{CNOT}} - C_{\text{raw}}$ between CNOT-corrected and raw surfaces in the integrable regime.

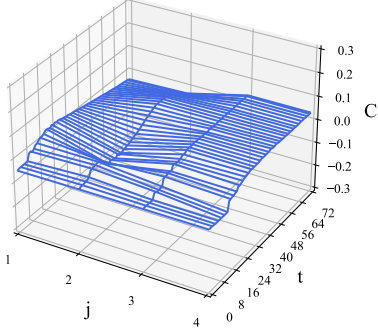


FIG. S5. Difference $C_{\text{TMEM}} - C_{\text{raw}}$ between measurement-corrected and raw surfaces in the chaotic regime.

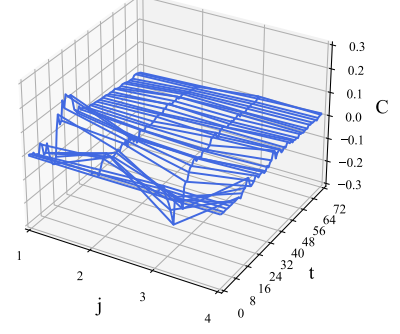


FIG. S7. Difference $C_{\text{CNOT}} - C_{\text{raw}}$ between CNOT-corrected and raw surfaces in the chaotic regime.

3. ERROR MITIGATION

In this work we correct all data for measurement errors using transition matrix error mitigation (TMEM)[60–64], and for incoherent CNOT errors using zero-noise extrapolation [65, 66]. In TMEM, the matrix T of transition probabilities between all prepared and observed classical states $x \in \{0, 1\}^n$ is initially measured. Then noisy data is corrected by minimizing $\|T p_{\text{corr}} - p_{\text{noisy}}\|_2^2$ subject to constraints $0 \leq p_{\text{corr}}(x) \leq 1$ and $\|p_{\text{corr}}\|_1 = 1$. Here $\|\cdot\|_2$ is the Euclidean norm and $\|\cdot\|_1$ is the ℓ_1 -norm. The effect of TMEM on the operator spreading data is shown in Figs. S4 and S5.

The CNOT error mitigation involves measuring each circuit together with a variant, obtained by replacing each CNOT in the original circuit by a logically equivalent CNOT³. Let $\Pr(x|m)$ be the probability of observing classical state x after implementing a circuit with each original CNOT replaced by m consecutive CNOTs.

Then let $\{\Pr(x|1)\}_x$ be a measured probability distribution for the original circuit, and $\{\Pr(x|3)\}_x$ be that for the CNOT³ variant. Assuming that the total incoherent CNOT error in the circuit occurs in proportion to the number of CNOTs implemented, one can use the two data points $\Pr(x|1)$ and $\Pr(x|3)$ to define a line with intercept

$$\Pr(x|0) := \frac{3\Pr(x|1) - \Pr(x|3)}{2}, \quad (\text{S2})$$

which defines a candidate correction. Here $m = 0$ means no incoherent CNOT error. If $0 \leq \Pr(x|0) \leq 1$ for all x , then we accept it as the corrected probability distribution:

$$\Pr(x)_{\text{corr}} = \Pr(x|0). \quad (\text{S3})$$

Otherwise we find the physical $\Pr(x)_{\text{corr}}$ closest to $\Pr(x|0)$ in Frobenius distance. The effect of CNOT noise extrapolation on the operator spreading data is shown in Figs. S6 and S7.

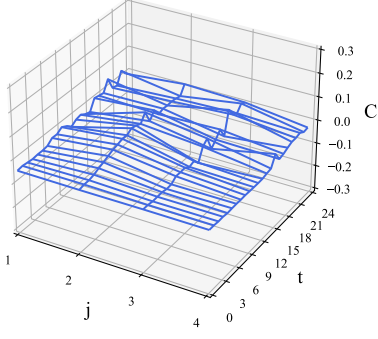


FIG. S8. Difference $C_{\text{corr}} - C_{\text{raw}}$ between fully corrected and raw surfaces in the integrable regime.

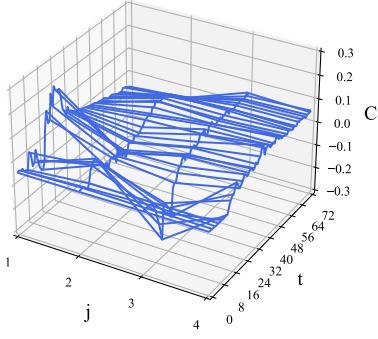


FIG. S9. Difference $C_{\text{corr}} - C_{\text{raw}}$ between fully corrected and raw surfaces in the chaotic regime.

The net effect of TMEM and CNOT noise extrapolation on the operator spreading data is shown in Figs. S8

If $j > 1$, we have

$$F_{1j}^0(t) = \sum_x \langle 0 \dots 0 | X_1(t) X_j | x \rangle \langle x | X_1(t) X_j | 0 \dots 0 \rangle \quad (\text{S9})$$

$$= \langle 0 \dots 0 | X_1(t) | 10 \dots 0 \rangle \langle 10 \dots 1_j \dots 0 | X_1(t) | 0 \dots 1_j \dots 0 \rangle \quad (\text{S10})$$

$$= \langle 0 \dots 0 | e^{iE_0 t} X_1 e^{-iHt} | 10 \dots 0 \rangle \langle 10 \dots 1_j \dots 0 | e^{iHt} X_1 e^{-iHt} | 0 \dots 1_j \dots 0 \rangle \quad (\text{S11})$$

$$= e^{2i(J+B_z)t} \langle 10 \dots 1_j \dots 0 | e^{iHt} X_1 e^{-iHt} | 00 \dots 1_j \dots 0 \rangle, \quad (\text{S12})$$

and there are three cases to consider: When $j = 2$, (S12) becomes

$$F_{12}^0(t) = e^{2i(J+B_z)t} \langle 110 \dots 0 | e^{iHt} X_1 e^{-iHt} | 01 \dots 0 \rangle \quad (\text{S13})$$

$$= e^{2i(J+B_z)t} \langle 110 \dots 0 | e^{i(E_0-2J-4B_z)t} X_1 e^{-i(E_0-4J-2B_z)t} | 01 \dots 0 \rangle \quad (\text{S14})$$

$$= e^{2i(J+B_z)t} e^{2i(J-B_z)t} \quad (\text{S15})$$

$$= e^{4iJt}, \quad (\text{S16})$$

and S9. When both error mitigations are applied to the raw operator spreading data, we obtain the surfaces in Figs. 4 and 5.

4. CLASSICAL OTOC

In the fixed-node approach, the absolute value of the OTOC is measured on the quantum processor but its phase is efficiently calculated from F_{ij}^0 , the OTOC (6) calculated with the classical Hamiltonian H^0 of (4). To calculate this phase, we need the energy of the n -qubit state $|0 \dots 0\rangle$, which is

$$E_0 = (n-1)J + nB_z. \quad (\text{S4})$$

Next we assume that $n \geq 3$. The energy of the single-excitation state $X_j|0 \dots 0\rangle = |0 \dots 1_j \dots 0\rangle$ is

$$E_{0 \dots 1_j \dots 0} = \begin{cases} E_0 - 2J - 2B_z & \text{if } j \in \{1, n\}, \\ E_0 - 4J - 2B_z & \text{else.} \end{cases} \quad (\text{S5})$$

We will also need the energy of the double-excitation state $|10 \dots 1_j \dots 0\rangle$, with $j \geq 2$, which is

$$E_{10 \dots 1_j \dots 0} = \begin{cases} E_0 - 2J - 4B_z & \text{if } j = 2, \\ E_0 - 4J - 4B_z & \text{if } j = n, \\ E_0 - 6J - 4B_z & \text{else.} \end{cases} \quad (\text{S6})$$

To calculate the OTOC we first write it as

$$F_{1j}^0(t) = \sum_x \langle 0 \dots 0 | X_1(t) X_j | x \rangle \langle x | X_1(t) X_j | 0 \dots 0 \rangle, \quad (\text{S7})$$

where $|x\rangle$ is a classical state with $x \in \{0, 1\}^n$. If $j = 1$ we have

$$\begin{aligned} F_{11}^0(t) &= \langle 0 \dots 0 | X_1(t) | 10 \dots 0 \rangle^2 \\ &= \langle 0 \dots 0 | e^{iE_0 t} X_1 e^{-i(E_0-2J-2B_z)t} | 10 \dots 0 \rangle^2 \\ &= e^{4i(J+B_z)t}, \end{aligned} \quad (\text{S8})$$

where we have used (S5).

where we have used (S6). When $2 < j < n$, (S12) becomes

$$F_{1j}^0(t) = e^{2i(J+B_z)t} \langle 10 \dots 1_j \dots 0 | e^{iHt} X_1 e^{-iHt} | 0 \dots 1_j \dots 0 \rangle \quad (\text{S17})$$

$$= e^{2i(J+B_z)t} \langle 10 \dots 1_j \dots 0 | e^{i(E_0-6J-4B_z)t} X_1 e^{-i(E_0-4J-2B_z)t} | 0 \dots 1_j \dots 0 \rangle \quad (\text{S18})$$

$$= e^{2i(J+B_z)t} e^{-2i(J+B_z)t} \quad (\text{S19})$$

$$= 1. \quad (\text{S20})$$

And when $j = n$, (S12) becomes

$$F_{1n}^0(t) = e^{2i(J+B_z)t} \langle 10 \dots 01 | e^{iHt} X_1 e^{-iHt} | 0 \dots 01 \rangle \quad (\text{S21})$$

$$= e^{2i(J+B_z)t} \langle 10 \dots 01 | e^{i(E_0-4J-4B_z)t} X_1 e^{-i(E_0-2J-2B_z)t} | 0 \dots 01 \rangle \quad (\text{S22})$$

$$= e^{2i(J+B_z)t} e^{-2i(J+B_z)t} \quad (\text{S23})$$

$$= 1. \quad (\text{S24})$$

Combining these results leads to the expression (7).

5. OTHER OTOCS

The operator spreading measurements in this work are based on the commutator

$$\text{tr}(\rho |[X_i(t), X_j(0)]|^2) \quad \text{with} \quad \rho = |0000\rangle\langle 0000|. \quad (\text{S25})$$

It is interesting to compare (S25) with alternative definitions. A common alternative is the infinite-temperature version

$$\text{tr}(\rho |[X_i(t), X_j(0)]|^2) \quad \text{with} \quad \rho = \frac{I}{d}, \quad (\text{S26})$$

where I is the $d \times d$ identity with $d = 2^n$. The operator spreading surfaces of Fig. 1, reevaluated with (S26), are shown in Fig. S10. These surfaces are ideal results obtained classically. Overall the spreading is similar to Fig. 1, but there are detailed differences.

It is also interesting to consider a pure state different than $|0\rangle^{\otimes n}$, such as $|+\rangle^{\otimes n}$. Figure S11 is based on the commutator

$$\text{tr}(\rho |[X_i(t), X_j(0)]|^2) \quad \text{with} \quad \rho = \frac{J}{d}, \quad (\text{S27})$$

where J is the $d \times d$ matrix of ones.

Finally, we consider the commutator

$$\text{tr}(\rho |[X_i(t), Y_j(0)]|^2) \quad \text{with} \quad \rho = |0000\rangle\langle 0000|, \quad (\text{S28})$$

which has a peak structure different from (S25) because $[X_i(t), Y_j(0)] \neq 0$ at time 0. The operator spreading surfaces of Fig. 1, reevaluated with (S28), are shown in Fig. S12.

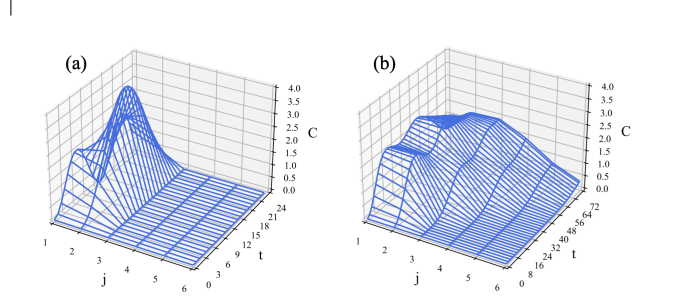


FIG. S10. Infinite-temperature commutator versus qubit position j and time t . (a) Integrable regime. The OTOC is calculated at times $t \in \{0, \tau, 2\tau, \dots, 24\tau\}$, with resolution $\tau = 0.06$, and time is plotted in units of τ . (b) Chaotic regime, calculated with $\tau = 0.03$. Parameters for both regimes are given in Table I. These results were obtained by classical simulation.

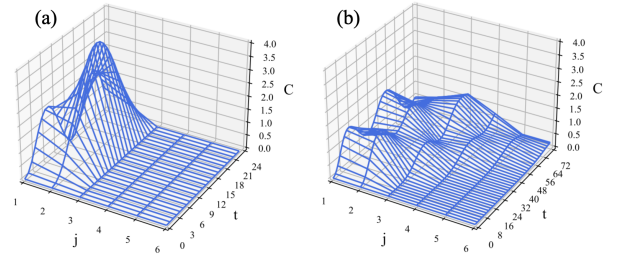


FIG. S11. Operator spreading in the $|+\rangle^{\otimes n}$ state, with other parameters the same as in Fig. S10.

- [S3] A. Kitaev, “A simple model of quantum holography,” talks given at the Kavli Institute for Theoretical Physics, University of California, Santa Barbara, U.S.A. (2015), <http://online.kitp.ucsb.edu/online/entangled15/kitaev/>.
- [S4] S. H. Shenker and D. Stanford, Journal of High Energy Physics **2014**, 67 (2014).
- [S5] J. Maldacena, S. H. Shenker, and D. Stanford, Journal of High Energy Physics **2016**, 1 (2016).
- [S6] S. Sachdev and J. Ye, Physical Review Letters **70**, 3339

* mgeller@uga.edu

† sornborg@lanl.gov

[S1] B. Swingle, Nature Physics **14**, 988 (2018).

[S2] P. Hayden and J. Preskill, Journal of High Energy Physics **9**, 120 (2007).

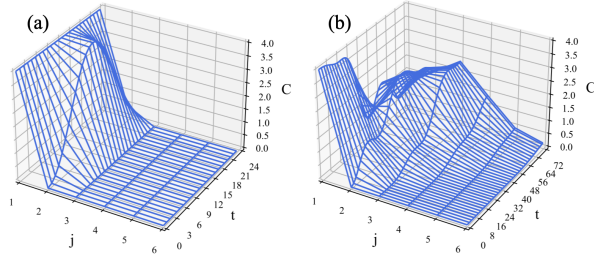


FIG. S12. Spreading of X_1 probed by Y_j , with other parameters the same as in Fig. S10..

- (1993).
- [S7] S. Sachdev, *Physical Review X* **5**, 041025 (2015).
 - [S8] R. Nandkishore and D. A. Huse, *Annu. Rev. Condens. Matter Phys.* **6**, 15 (2015).
 - [S9] D. A. Abanin, E. Altman, I. Bloch, and M. Serbyn, *Reviews of Modern Physics* **91**, 021001 (2019).
 - [S10] A. Larkin and Y. N. Ovchinnikov, *Sov Phys JETP* **28**, 1200 (1969).
 - [S11] L. García-Álvarez, I. Egusquiza, L. Lamata, A. Del Campo, J. Sonner, and E. Solano, *Physical Review Letters* **119**, 040501 (2017).
 - [S12] N. Y. Halpern, B. Swingle, and J. Dressel, *Physical Review A* **97**, 042105 (2018).
 - [S13] B. Swingle and N. Y. Halpern, *Physical Review A* **97**, 062113 (2018).
 - [S14] Y.-L. Zhang, Y. Huang, X. Chen, *et al.*, *Physical Review B* **99**, 014303 (2019).
 - [S15] B. Yoshida and N. Y. Yao, *Physical Review X* **9**, 011006 (2019).
 - [S16] R. Babbush, D. W. Berry, and H. Neven, *Physical Review A* **99**, 040301 (2019).
 - [S17] J. R. G. Alonso, N. Y. Halpern, and J. Dressel, *Physical Review Letters* **122**, 040404 (2019).
 - [S18] B. Vermersch, A. Elben, L. M. Sieberer, N. Y. Yao, and P. Zoller, *Physical Review X* **9**, 021061 (2019).
 - [S19] C. B. Dağ, K. Sun, and L.-M. Duan, *Physical Review Letters* **123**, 140602 (2019).
 - [S20] B. Yan, L. Cincio, and W. H. Zurek, *Physical Review Letters* **124**, 160603 (2020).
 - [S21] R. Belyansky, P. Bienias, Y. A. Kharkov, A. V. Gorshkov, and B. Swingle, *Physical Review Letters* **125**, 130601 (2020).
 - [S22] B. Yan and N. A. Sinitsyn, *Physical Review Letters* **125**, 040605 (2020).
 - [S23] A. Touil and S. Deffner, *PRX Quantum* **2**, 010306 (2021).
 - [S24] C.-J. Lin and O. I. Motrunich, *Physical Review B* **97**, 144304 (2018).
 - [S25] S. Xu and B. Swingle, *Physical Review X* **9**, 031048 (2019).
 - [S26] E. M. Fortes, I. García-Mata, R. A. Jalabert, and D. A. Wisniacki, *Physical Review E* **100**, 042201 (2019).
 - [S27] E. M. Fortes, I. García-Mata, R. A. Jalabert, and D. A. Wisniacki, *EPL (Europhysics Letters)* **130**, 60001 (2020).
 - [S28] Z. Holmes, A. Arrasmith, B. Yan, P. J. Coles, A. Albrecht, and A. T. Sornborger, *Physical Review Letters* **126**, 190501 (2021).
 - [S29] F. D. M. Haldane, *Physical Review Letters* **50**, 1153 (1983).
 - [S30] B. Swingle, G. Bentsen, M. Schleier-Smith, and P. Hayden, *Physical Review A* **94**, 040302 (2016).
 - [S31] G. Zhu, M. Hafezi, and T. Grover, *Physical Review A* **94**, 062329 (2016).
 - [S32] N. Y. Yao, F. Grusdt, B. Swingle, M. D. Lukin, D. M. Stamper-Kurn, J. E. Moore, and E. A. Demler, *arXiv preprint arXiv:1607.01801* (2016).
 - [S33] N. Y. Halpern, *Physical Review A* **95**, 012120 (2017).
 - [S34] C. Cirstoiu, Z. Holmes, J. Iosue, L. Cincio, P. J. Coles, and A. Sornborger, *npj Quantum Information* **6**, 1 (2020).
 - [S35] B. Commeau, M. Cerezo, Z. Holmes, L. Cincio, P. J. Coles, and A. Sornborger, *arXiv preprint arXiv:2009.02559* (2020).
 - [S36] J. Gibbs, K. Gili, Z. Holmes, B. Commeau, A. Arrasmith, L. Cincio, P. J. Coles, and A. Sornborger, *arXiv preprint arXiv:2102.04313* (2021).
 - [S37] M. R. Geller, Z. Holmes, P. J. Coles, and A. Sornborger, *arXiv preprint arXiv:2104.03295* (2021).
 - [S38] K. Bharti and T. Haug, *arXiv preprint arXiv:2010.05638* (2020).
 - [S39] J. W. Z. Lau, K. Bharti, T. Haug, and L. C. Kwek, *arXiv preprint arXiv:2101.07677* (2021).
 - [S40] T. Haug and K. Bharti, *arXiv preprint arXiv:2011.14737* (2020).
 - [S41] S. Barison, F. Vicentini, and G. Carleo, *arXiv preprint arXiv:2101.04579* (2021).
 - [S42] C. J. Trout, M. Li, M. Gutiérrez, Y. Wu, S.-T. Wang, L. Duan, and K. R. Brown, *New Journal of Physics* **20**, 043038 (2018).
 - [S43] S. Endo, J. Sun, Y. Li, S. C. Benjamin, and X. Yuan, *Physical Review Letters* **125**, 010501 (2020).
 - [S44] Y.-X. Yao, N. Gomes, F. Zhang, T. Iadecola, C.-Z. Wang, K.-M. Ho, and P. P. Orth, *arXiv preprint arXiv:2011.00622* (2020).
 - [S45] M. Benedetti, M. Fiorentini, and M. Lubasch, *arXiv preprint arXiv:2009.12361* (2020).
 - [S46] J. Li, R. Fan, H. Wang, B. Ye, B. Zeng, H. Zhai, X. Peng, and J. Du, *Physical Review X* **7**, 031011 (2017).
 - [S47] M. Gärttner, J. G. Bohnet, A. Safavi-Naini, M. L. Wall, J. J. Bollinger, and A. M. Rey, *Nature Physics* **13**, 781 (2017).
 - [S48] E. J. Meier, F. A. An, B. Gadway, *et al.*, *Physical Review A* **100**, 013623 (2019).
 - [S49] X. Nie, Z. Zhang, X. Zhao, T. Xin, D. Lu, and J. Li, *arXiv preprint arXiv:1903.12237* (2019).
 - [S50] K. A. Landsman, C. Figgatt, T. Schuster, N. M. Linke, B. Yoshida, N. Y. Yao, and C. Monroe, *Nature* **567**, 61 (2019).
 - [S51] M. Blok, V. Ramasesh, T. Schuster, K. O'Brien, J. Kreikebaum, D. Dahlen, A. Morvan, B. Yoshida, N. Yao, and I. Siddiqi, *Physical Review X* **11**, 021010 (2021).
 - [S52] B. Chen, X. Hou, F. Zhou, P. Qian, H. Shen, and N. Xu, *arXiv preprint arXiv:2001.06333* (2020).
 - [S53] M. Niknam, L. F. Santos, and D. G. Cory, *Physical Review Research* **2**, 013200 (2020).
 - [S54] X. Mi, P. Roushan, C. Quintana, S. Mandra, J. Marshall, C. Neill, F. Arute, K. Arya, J. Atalaya, R. Babbush, *et al.*, *arXiv preprint arXiv:2101.08870* (2021).
 - [S55] J. Braumüller, A. H. Karamlou, Y. Yanay, B. Kannan,

- D. Kim, M. Kjaergaard, A. Melville, B. M. Niedzielski, Y. Sung, A. Vepsäläinen, *et al.*, arXiv preprint arXiv:2102.11751 (2021).
- [S56] F. Chen, Z.-H. Sun, M. Gong, Q. Zhu, Y.-R. Zhang, Y. Wu, Y. Ye, C. Zha, S. Li, S. Guo, *et al.*, arXiv preprint arXiv:2102.08587 (2021).
- [S57] M. K. Joshi, A. Elben, B. Vermersch, T. Brydges, C. Maier, P. Zoller, R. Blatt, and C. F. Roos, *Physical Review Letters* **124**, 240505 (2020).
- [S58] Q. Zhu, Z.-H. Sun, M. Gong, F. Chen, Y.-R. Zhang, Y. Wu, Y. Ye, C. Zha, S. Li, S. Guo, *et al.*, arXiv preprint arXiv:2101.08031 (2021).
- [S59] See Supplementary Information for additional data and analysis.
- [S60] F. B. Maciejewski, Z. Zimborás, and M. Oszmaniec, *Quantum* **4**, 257 (2020).
- [S61] B. Nachman, M. Urbanek, W. A. de Jong, and C. W. Bauer, *npj Quantum Information* **6**, 1 (2020).
- [S62] K. E. Hamilton, T. Kharazi, T. Morris, A. J. McCaskey, R. S. Bennink, and R. C. Pooser, in *2020 IEEE International Conference on Quantum Computing and Engineering (QCE)* (IEEE, 2020) pp. 430–440.
- [S63] S. Bravyi, S. Sheldon, A. Kandala, D. C. McKay, and J. M. Gambetta, *Physical Review A* **103**, 042605 (2021).
- [S64] M. R. Geller and M. Sun, *Quantum Science and Technology* **6**, 025009 (2021).
- [S65] K. Temme, S. Bravyi, and J. M. Gambetta, *Phys. Rev. Lett.* **119**, 180509 (2017).
- [S66] E. F. Dumitrescu, A. J. McCaskey, G. Hagen, G. R. Jansen, T. D. Morris, T. Papenbrock, R. C. Pooser, D. J. Dean, and P. Lougovski, *Phys. Rev. Lett.* **120**, 210501 (2018).